

Hardware-efficient megapixel per second coherent soliton microcomb ranging

Anton Lukashchuk, Johann Riemensberger, Maxim Karpov, Junqiu Liu, and Tobias J. Kippenberg*

Laboratory of Photonics and Quantum Measurements (LPQM),

Swiss Federal Institute of Technology Lausanne (EPFL), CH-1015 Lausanne, Switzerland

(Dated: February 28, 2025)

Laser based ranging (LiDAR) - already ubiquitously used in robotics, industrial monitoring, or geodesy - is a key sensor technology for future autonomous driving [1], and has been employed in nearly all successful implementations of autonomous vehicles to date. Coherent laser ranging [2, 3] in contrast to time-of-flight approaches, allows long range detection, operates eye safe, is immune to crosstalk and moreover yields simultaneous velocity and distance information, greatly simplifying object classification. Yet for actual deployment in vehicles, video frame-rate requirements for object detection, classification and sensor fusion mandate megapixel per second measurement speed. Such pixel rates are not possible to attain with current coherent single laser-detector architectures at high definition range imaging [4], and make parallelization essential. Recent advances based on photonic chip based microcombs [5, 6] offer a solution to reduced complexity on the transmitter side [7], yet a megapixel class real-world parallel coherent LiDAR has not been demonstrated, and is still impeded by the arduous requirements of large banks of detectors and digitizers on the receiver side, that need to be integrated on chip [8]. Here we report hardware efficient coherent laser ranging at megapixel per second imaging rates. This is achieved using a novel concept for massively parallel coherent laser ranging that requires only a single laser and a single photoreceiver, yet achieves simultaneous recording of more than 64 channels with distance and velocity measurements each - attaining an unprecedented 5 megapixel per second rate. Coherently driving two photonic chip-based microcombs with different repetition rates, and heterodyning multiple comb lines on a single telecommunication coherent 'intradyne' receiver with 10 GHz detection bandwidth yields a complex beat note spectrum [9] containing both distance and velocity information of all individual ranging channels at particular radio frequencies, on a single detector, thereby alleviating the need to individually separate, detect and digitize distinct channels. The reported LiDAR implementation is hardware-efficient, compatible with photonic integration and demonstrates the significant advan-

tages of acquisition speed, complexity and cost benefits afforded by the convergence of optical telecommunication and metrology technologies.

Three dimensional (3D) imaging based on lasers (LiDAR) is ubiquitously used in numerous applications, ranging from industrial specimen inspection, to airborne imaging for cartography of geological sites [10] and urban-planning, to satellite-based applications in space. In recent years, driven by the large investments and development under way in autonomous driving, combined with advances in drone technology there has been a surge of interest in more sophisticated laser ranging system, in particular LiDAR. LiDAR allows to maintain excellent angular resolution at long range, works reliably in a variety of weather, illumination and target conditions that impede direct camera imaging and is a mainstay in nearly all successful demonstrations of highly autonomous vehicles to date [11]. While most commercial implementations of LiDAR employ incoherent detection of the intensity of reflected light, coherent detection of the back-reflected signal using a copy of the transmitted optical waveform allows a more robust detection that is intrinsically resilient to crosstalk and interference from ambient sunlight and, importantly, gives both distance and velocity via the Doppler effect for each pixel, significantly facilitating classification. For these reasons FMWC LiDAR is widely regarded as a superior laser ranging technology at long distance for autonomous driving. The key challenge to harvesting the inherent advantages of FMCW LiDAR for 3D imaging is to overcome the frame-rate acquisition bottleneck that if not parallelized by the means of microresonator frequency combs [7] or electro-optical combs [12], is imposed by tuneable diode laser sources that trade-off tunability versus linewidth [13] and spurious Doppler shifts of mechanical scanning mirrors, which necessitate for inertial free scanning solutions. Parallelization of coherent LiDAR is essential for future deployment, and is already widely employed in time of flight LiDAR, with up to 128 simultaneous channels. A video rate (30 Hz) frame rate, with 600×300 pixel images, requires more than 5 MegaPixel/second measurement rates. Such large frame rates cannot be attained by increasing measurement speed due to limitations imposed by mechanical scanning, as well as pixel dwell time, i.e. signal to noise ratio. A manifold of solutions for mechanical component free scanning based on photonic switching networks [8], focal plane arrays [14], spectrally encoded spatial scanning with broadband light sources [4, 15] or

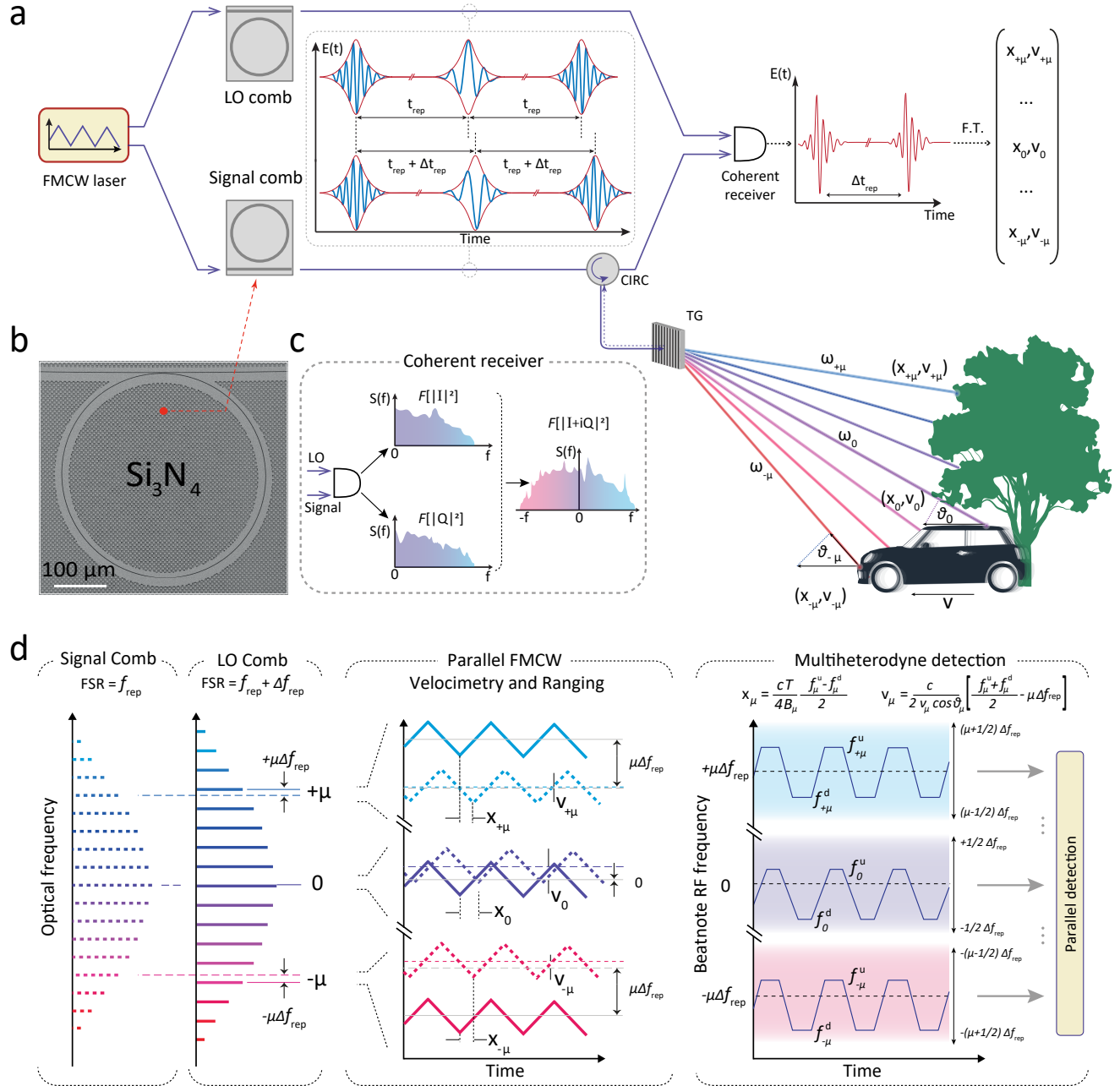


FIG. 1. Multiheterodyne parallelization of coherent laser ranging a) Architecture of the multiheterodyne parallel FMCW LiDAR. A single pump laser with triangular frequency modulation is split, and drives two distinct optical microresonators with slightly different radii, which serve as signal and local oscillator (LO) in the experiment. The signal comb is spatially dispersed over the target area using diffractive optics. Each signal comb tooth μ represents an independent FMCW ranging channel measuring distance x_μ and velocity v_μ . All channels are simultaneously superimposed with the LO comb on a coherent receiver. Interferogram is recorded and processed via time-frequency analysis to retrieve distance x_μ and velocity v_μ . b) Electron microscope picture of $228.43 \mu\text{m}$ Si_3N_4 microring resonator. c) Complex RF waveform is retrieved by the means of phase diversity detection. d) Principle of multiheterodyne ranging and velocimetry. Signal and LO combs have repetition rates f_{rep} of 98.90 GHz and 99.39 GHz, respectively. The reflected signal comb light is both time delayed, and frequency shifted due to the Doppler effect. Beat notes of consecutive comb tooth pairs are spaced 490 MHz in the RF spectrum. Triangular frequency modulation maps the distance of target objects to two RF beat notes, f_μ^d and f_μ^u , spaced around the center frequency of the multiheterodyne channel $\mu \cdot f_{\text{rep}}$ offset by the Doppler shift caused by the relative velocity of LiDAR transmitter and target.

optical phased arrays [16] have been demonstrated, which are compatible with MPixel/second frame rate. Yet to date, mega-pixel rate coherent LiDAR have not been demonstrated. Recently the parallelization of FMCW has been shown to be possible using using photonic integrated microcombs [5, 6] (although electro-optical combs are equally suitable [12, 17]). These sources are based on the microresonator soliton's ability to faithfully transfer the time-frequency characteristics of a single well controlled FMCW pump laser to all comb teeth at modulation speeds up to 10 MHz with mode spacing of 100 GHz that can be readily multiplexed [7]. The large comb spacing facilitates the spatial separation of the comb teeth with diffractive optics and each tooth can *independently* and *simultaneously* measure the distance and velocity of a target in a truly parallel fashion, if all channels are simultaneously detected. The latter however is a key challenge.

To unlock the potential of massively parallel FMCW ranging, requires overcoming the challenge that the number of optical balanced photo-receivers, amplifiers and analog-to-digital converters is identical to the channel number that is employed, which necessitates custom, large-area silicon photonic solutions [8, 14] in addition to multiplexers. Moreover, single channel LiDAR architectures cannot benefit from existing silicon photonics transceiver based coherent receivers [18], which have been developed for high bandwidth (GHz) electrical signals - in contrast to the low frequency signals generated in coherent LiDAR.

Concept of hardware efficient megapixel coherent ranging

Here we overcome these limitations and demonstrate a hardware-efficient massively parallel coherent FMCW LiDAR transceiver based on multiheterodyne mixing of two photonic chip-based soliton microcombs on a single coherent photoreceiver (cf. Fig. 1), enabling *bona fide* 5.6 Mega-Pixel/second measurement rate, with more than 64 simultaneous channels. Our approach is a swept frequency version of multiheterodyne detection [19] of optical frequency combs, commonly referred to as dual-comb spectroscopy, a technique which has attained widespread attention and application in (nonlinear) optical spectroscopy [20, 21], distance measurement [22–24], two-way time-frequency transfer [25] and microwave photonics [26], multi-dimensional spectroscopy [27] and coherent anti-Stokes Raman imaging [28]. By radio-frequency multiplexing, our approach enables to decode all individual low frequency (MHz bandwidth) LiDAR channels using a single high speed (GHz) coherent 'intradynic' detector.

In our experiments, we utilize a single highly coherent FMCW laser ($\mu = 0$) that is amplified, split and

coupled into two size-mismatched photonic chip based integrated Si_3N_4 [29] microring resonators (cf. Fig. 1b) driving two dissipative Kerr solitons [5]. As recently shown, fast frequency tuning of the pump laser within the soliton existence range, retains the solitonic state [7] in both resonators. The rapid frequency modulation is encoded onto the carrier-envelope frequency f_{ceo} of the pulse, while the pulse repetition rate f_{rep} remains almost constant. The schematic of our architecture is depicted in Fig. 1a. The amplified signal comb is dispersed using a transmission grating (966 lines/mm). In the frequency domain (cf. Fig. 1c), we obtain two soliton microcombs with slightly different comb line spacing Δf_{rep} where each comb line inherits the pump laser frequency modulation. Multiheterodyne mixing of the reflected signal comb with the local oscillator (LO) comb (cf. Fig. 1c), using a *single* coherent photoreceiver records the complex RF spectrum (cf. Fig. 1d), which allows the distance x_μ and velocity v_μ to be recorded for *each comb line* μ *simultaneously*. In comparison to conventional FMCW LiDAR [30], multiheterodyne detection modifies the formulas to calculate (x_μ, v_μ) from the beat notes f_μ^u, f_μ^d measured during the up- and down-chirping of the FMCW laser, because the intermediate frequency is no longer at baseband. Instead, consecutive channels in the radio-frequency (RF) domain are separated by the difference in comb line spacing Δf_{rep} . To mitigate the degeneracy in optical detection between $+\mu$ and $-\mu$ comb lines located symmetric about the pump ($\mu = 0$), we employ a phase diversity receiver architecture [31] (widely used in coherent telecommunication) and measure both the in-phase (I) and quadrature (Q) components of the multiheterodyne beat note (cf. Fig. 1c). The distinction between positive and negative frequencies in the multiheterodyne beat spectrum is obtained via Fourier transform of the complex field amplitude $I+iQ$ [32]. The Doppler shift is observed by a deviation of the beat note pattern from $\mu \cdot \Delta f_{\text{rep}}$ and non-zero detection distance translates into a splitting of the RF beat note

$$\begin{aligned} x_\mu &= \frac{cT}{4B_\mu} \cdot \frac{f_\mu^u - f_\mu^d}{2} \\ v_\mu &= \frac{c}{2v_\mu \cos\theta_\mu} \cdot \left[\frac{f_\mu^u + f_\mu^d}{2} - \mu \Delta f_{\text{rep}} \right], \end{aligned} \quad (1)$$

where $v_\mu \cos\theta_\mu$ is a projection of the target velocity on a comb line.

Figure 2a depicts optical spectra of LO and signal combs which feature 99.39 GHz and 98.9 GHz repetition rates, i.e. a 490 MHz difference, respectively. We generate simultaneously two DKS from a single triangularly chirped laser, with an amplitude $B = 1.5$ GHz and period $T = 10 \mu\text{s}$. This is achieved by thermally tuning the two pump resonances into degeneracy, such that their trajectories in the soliton existence range are similar (cf. Fig 2 b). The red and blue shaded spectral regions indicate

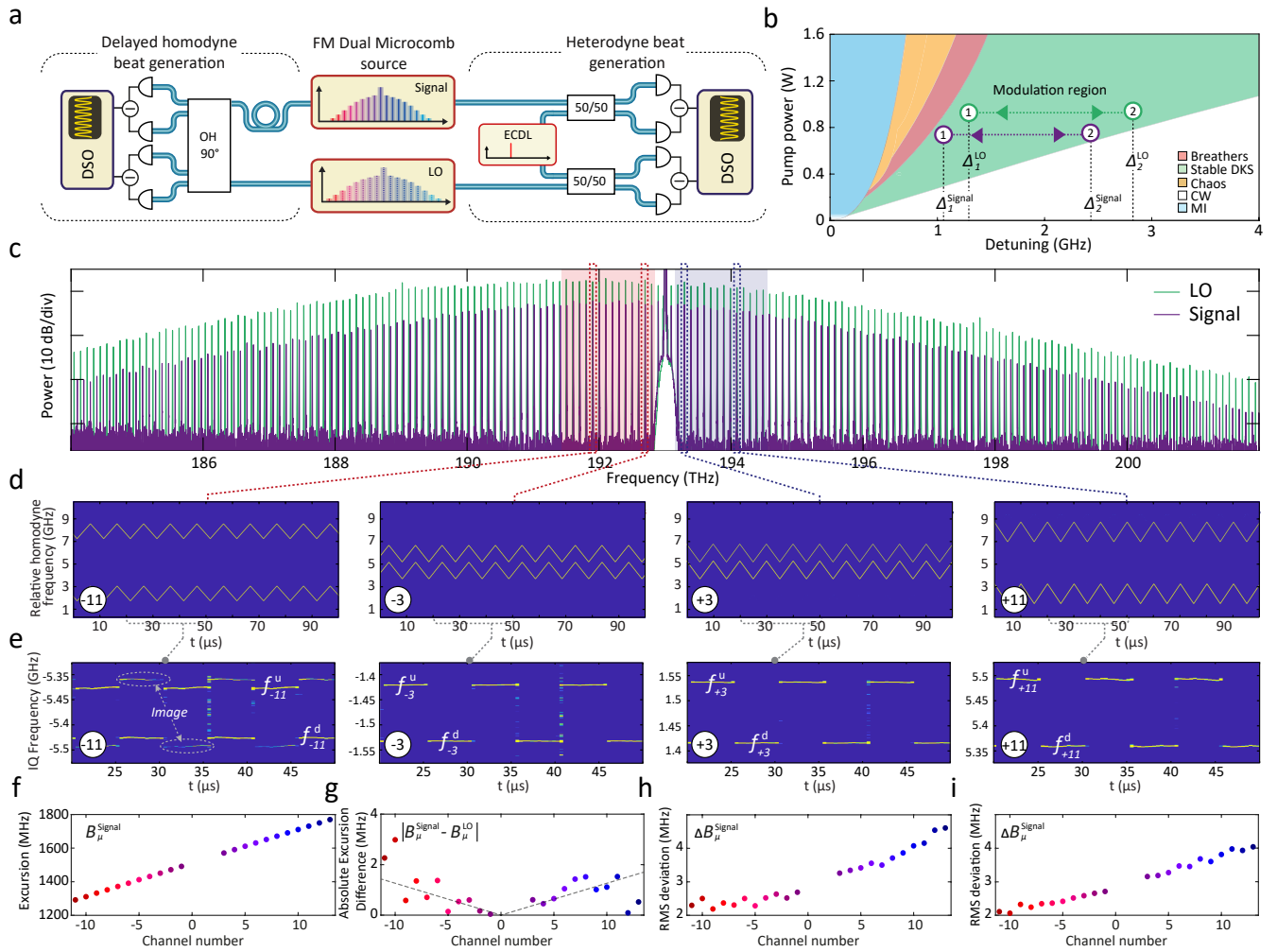


FIG. 2. Coherent detection of multiple FMCW laser channels a) Optical setup for heterodyne and delayed homodyne beat note measurement. The signal microcomb is delayed and mixed in a 90° optical hybrid and superimposed with the local oscillator (LO) microcomb on a pair of balanced photoreceivers for delayed homodyne beat frequency generation. Alternatively, the tuning of individual comb line pairs are characterized by heterodyne mixing with an external cavity diode laser (ECDL). b) Soliton microcomb stability chart. Optical resonances are thermally tuned to superimpose the laser-cavity detuning regions of stable soliton generation (green shaded). MI: modulation instability; CW continuous-wave; c) Optical spectra of signal and LO combs featuring a slight offset in repetition rate. The blue(red) shading highlights positive(negative) channels ($\mu = 0$ denotes the pump laser) used in LiDAR experiments limited by the available amplifier bandwidth and amplified spontaneous emission noise. d) Time-frequency map of heterodyne beat spectroscopy at the ± 3 and ± 11 channels. ENBW 2.45 MHz. e) Time-frequency map of delayed homodyne beat spectroscopy. ENBW 2.45 MHz. f) Channel-dependent frequency excursion bandwidth at 100-kHz modulation frequency. g) Channel-dependent absolute excursion difference of signal and LO combs. h,i) Channel-dependent RMS deviation from a perfect triangular frequency chirp for LO and signal.

the comb lines that are evaluated in the ranging experiment. We filter out the pump and ± 1 sidebands of the LO to remove excess amplified spontaneous emission noise around the laser pump. The pump laser frequency is modulated using a dual Mach-Zehnder modulator biased to single sideband modulation, which in turn is driven by a voltage-controlled digitally predistorted linearized triangular waveform. First, a heterodyne beat note is obtained by superimposing the frequency combs individually with an external-cavity diode laser onto two balanced photoreceivers (BPD). The resulting signals are added

and analyzed by short-time Fourier transform. Fig. 2d shows the laser frequency of two individual comb teeth of the two simultaneously chirped local oscillator and signal microcomb for channels $\mu = \pm 3, \pm 11$, highlighting the similarity and relative spacing of the frequency modulation pattern. The delayed homodyne beat note spectrum for the same channels is depicted in Fig. 2e. Image peaks are related to imperfect phase compensation in IQ-detection, which is outlined in detail in the methods section. From a technical point of view, one difference to our earlier demonstration of single comb parallel FMCW Li-

DAR [7] is that the signal and LO splitting takes place before soliton generation and the nonlinear microresonators are part of the measurement Mach-Zehnder interferometer (MZI). This enables to employ dual comb heterodyne detection on a single photoreceiver, which is not possible using a single comb only. The maximum number of LiDAR channels is limited by the optical amplification and coherent receiver bandwidths B_{pd} . The latter limitation reads as $\mu\Delta f_{rep} < B_{pd}$ and can be overcome by reducing the repetition rate difference Δf_{rep} with the trade-off of a reduced distance ambiguity range. The channel dependency of the frequency excursion B_μ (cf. Fig. 2f) is related to the soliton self-frequency shift induced by intrapulse Raman scattering [33, 34] and dispersive wave recoil [35, 36] and ranges from 1.3 GHz to 1.8 GHz which corresponds to a native distance resolution $\Delta x_\mu = c/2B_\mu$ of 12 cm to 8 cm. The requirement of high mutual coherence between the signal and LO combs and their large optical channel spacing is ensured without the need for external phase locking. Our degenerate pumping scheme and the excellent uniformity of the photonic resonators provide most equal transduction of the pump laser frequency modulation to both combs, which is also reflected in the low and equal nonlinearity of the comb tooth chirps in both combs (cf. Fig. 2h,i and methods section).

Megapixel-per-second coherent ranging

To demonstrate the capabilities of dual-comb massively parallel coherent imaging, we perform proof-of-principle parallel ranging experiments. The setup is depicted in Fig. 3a. The soliton microcombs are amplified in erbium-doped fiber amplifiers (EDFA). The target is composed of three chess figures (queen, king and pawn) placed approximately ~ 1 m in front of the beam-splitter and optical transmission grating. A single-axis galvanometric mirror is used for beam scanning in the vertical direction. Fig. 3c depicts the optical spectrum of the signal comb amplified up to ~ 10 dBm per comb line of optical power. Fig. 3b depicts the complex RF spectrum obtained by Fourier transform of the I+iQ signal from the coherent receiver of one period acquisition time ($10 \mu\text{s}$). Blue and red shadings highlight positive $\mu > 0$ and negative $\mu < 0$ frequency comb teeth with respect to the pump laser frequency. The details of the multichannel data segmentation filtering and IQ phase and amplitude imbalance compensation are outlined in the methods section. Two different projections of the 3D-imaging results for a scan of 136 vertical angles across the set of chess figures are depicted in Fig. 3d,e. A line of 28 pixels is recorded during a single $10 \mu\text{s}$ triangular laser chirp, which equates to a *true*, i.e. *bona fide* 2.8 MPix/s coherent distance sampling rate at the sampling oscilloscope. We emphasize that this operation is to well be distinguished from experiments, which do not detect,

digitize and process each individual channel that is demultiplexed, and are thus reporting aggregated data or sampling rates only [7].

Dense massively parallel coherent ranging

In a second proof-of-principle experiment, we demonstrate dense coherent hardware-efficient parallel velocimetry with our dual frequency-modulated soliton microcomb platform at even higher rates of 6.4 megapixel per second. Lowering the repetition rate to 35 GHz only, illustrates the advantage of the dual comb approach, which alleviates the need to operate at large line spacings compatible with multiplexers and facilitates mode spacing related limitations of channel isolation. To this end, we employ two low repetition rate solitons microcomb operating at Δf_{rep} of 35 GHz allowing to have more than 60 channels within our EDFA gain window. While spectral compression of the microcomb from 99 GHz to 35 GHz does limit the triangular chirp frequency excursion to 700 MHz (while preserving the same pump power), this does not limit the accuracy of Doppler velocimetry and we can retain the 100 kHz modulation frequency. The optical spectra of the signal and LO solitons are shown in Fig. 4a. The inset highlights the repetition rate offset Δf_{rep} of only ~ 140 MHz. The signal comb is dispersed by the same transmission grating along the circumference of a 20 mm flywheel rotating at 230 Hz (cf. Fig. 4b). The pump channel is approximately aligned at the center of the flywheel such that negative channels record an approaching target and positive channels a receding target. The time frequency maps of the complex spectrum for the $\mu = \pm 6, \pm 26$ channels are plotted in Fig. 4c and the dashed red lines highlight the baseband frequencies of multi-heterodyne detection equal to $\mu\Delta f_{rep}$. We calculate the velocities by computing the mean deviation of the beat notes from the equivalent baseband and depict the results in Fig. 4d. Open circles depict the results after analyzing a single scan period, while the filled circles depict the results obtained over 5 frames averaging. On average, we attained 56 pixel detections over one period resulting in 5.6 MPix/s, i.e. actually detected, velocity and distance information acquisition speed. The grey circles depict the velocimetry result for the static wheel, while the measurement uncertainty is depicted in Fig. 4d middle panel and is limited by the mechanical vibrations of the flywheel. The distance measurement is depicted in Fig. 4d bottom panel. With recent demonstrations of DKS in low-repetition rate microresonators [37, 38] the approach could readily exceed 10 MPix/s.

Summary

In summary, we have demonstrated a hardware-efficient implementation of a massively parallel coherent

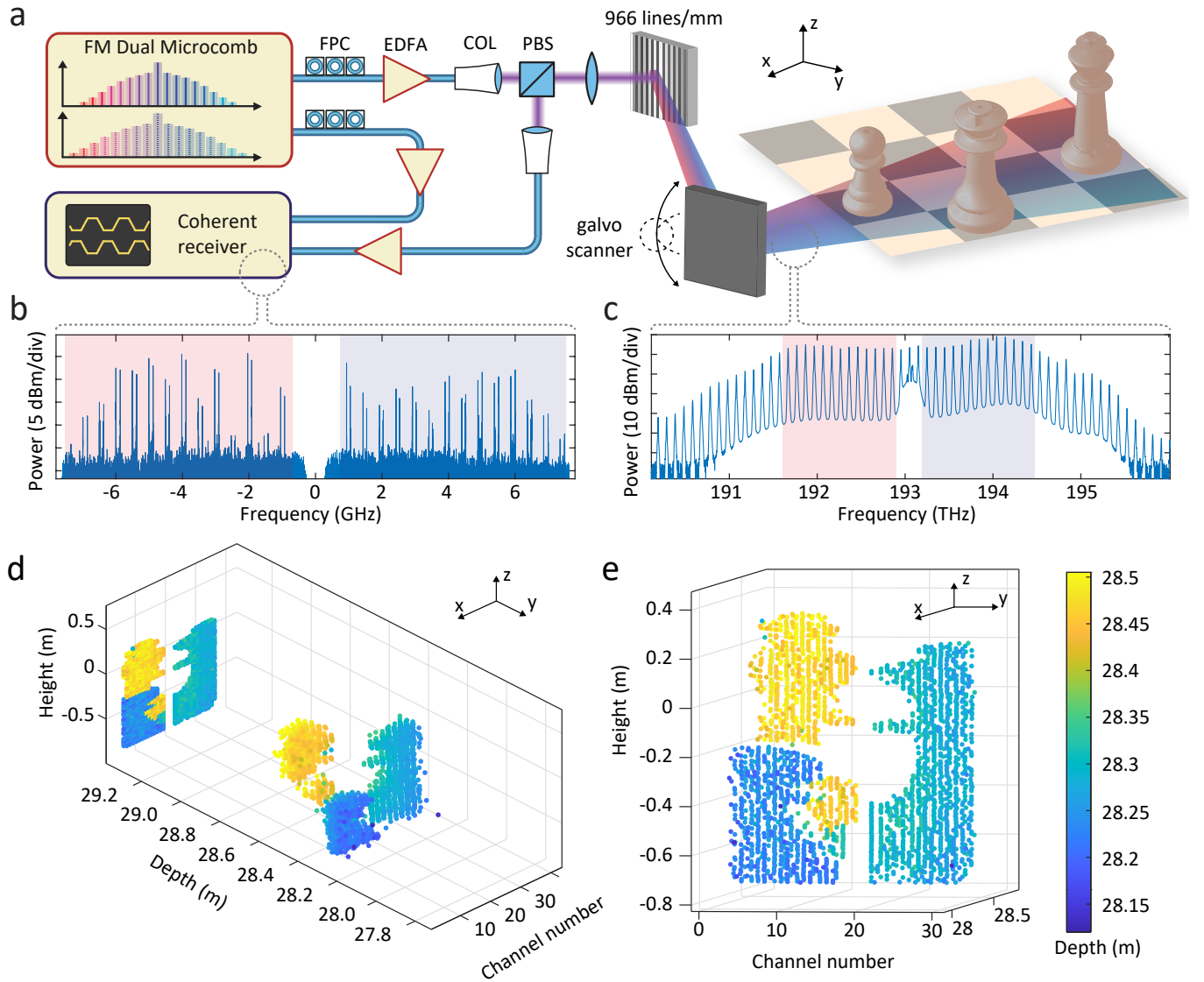


FIG. 3. **Dual comb parallel 3D imaging at 2.8 megapixel per second** a) Experimental setup. The amplified signal comb is dispersed in free-space by a 966 lines/mm transmission grating and vertical scanning is provided by a mirror galvanometer. FPC: Fiber polarization controller; COL: collimator; PBS: Polarizing beamsplitter. b) Power spectral density of the electrical signal obtained at the coherent receiver highlighting 28 FMCW channels. The red and blue shading highlights signals obtained from negative and positive channel numbers, respectively. c) Optical spectrum used for 3D imaging. The red and blue shaded regions correspond to the signal plotted in panel b). d,e) Point clouds of the three chess figures obtained during a scan (28×136 points) of the mirror galvanometer.

laser ranging scheme based on multiheterodyne detection on a single coherent receiver attaining multi-megapixel per second rates. Two integrated soliton microcombs driven by the same chirped pump laser provide a minimalist implementation of the dual chirped-comb system. The approach is free of channel separation, photo-detection and processing of individual channels. While the approach comes at the expense of reduced SNR due to the multiheterodyne detection penalty [39] (outlined in the methods section), the latter is compensated for by the absence of multiplexers or photonic integrated so-

lutions for detection of individual channels, which typically exhibit significant insertion loss. When combined with phase arrays, or other compact non-inertial scanning solutions, our approach provides a route to field deployable MPix/s LiDAR systems, that provide sufficient frame rate to allow video rate 3D imaging. Moreover, high bandwidth I-Q detectors are already offered commercially in silicon photonics - making our approach fully compatible with photonic integration. Since multiplexers are not required in our approach, it allows utilization of arbitrary, and in particular very dense, frequency

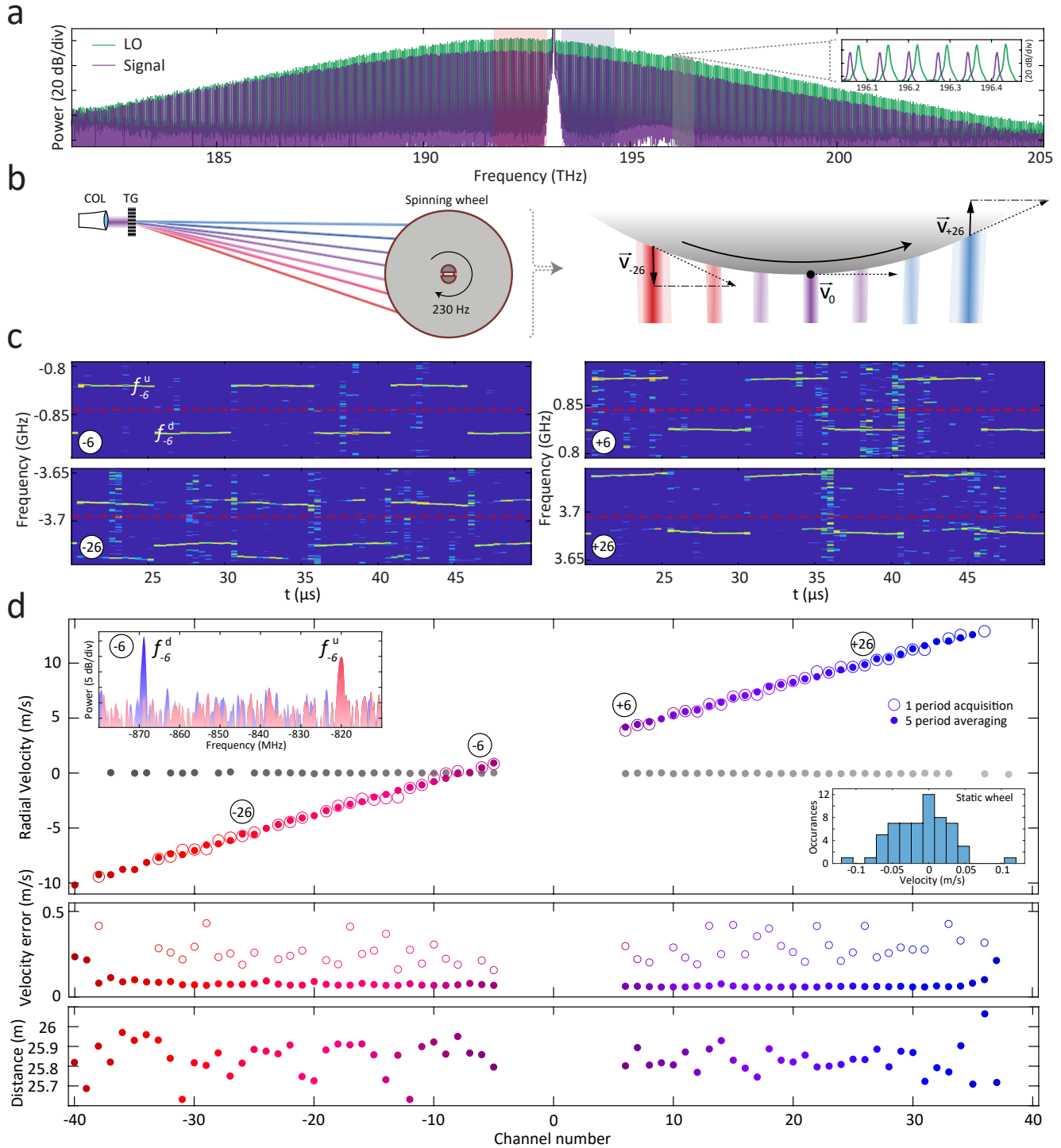


FIG. 4. **Dense dual comb parallel velocimetry measurement at 6.4 Mega-Pixel/second rates** a) Optical spectra of the 35 GHz dual FMCW combs. b) Schematic illustration of the flywheel section irradiated by the signal comb lines. (Left) COL: Collimator; TG: transmission grating. (Right) The projections of the velocity v_μ of the wheel onto the comb lines. c) Time-frequency map featuring an offset of the mean beat frequency from the $\mu\Delta f_{\text{rep}}$ due to the Doppler shift. ENBW 2.45 MHz. d) (Top) Multichannel velocity measurement for the flywheel rotating at around 200 Hz for a single 10 μ s scan (open circles) and five frame stacking (filled circles). Grey data points show velocimetry results for the static wheel. (Middle) Error of velocimetry for single scan and 5 frame stack. (Bottom) Ranging results for five frame stacking.

comb channel spacings. Broadband semiconductor optical amplifiers, which could be co-integrated on the silicon substrate [40], can be used instead of erbium-doped fiber amplifiers (EDFA). Such broadband amplification allows increasing comb repetition rate while maintaining channel count, leading to higher soliton comb line power and relaxing the requirements on the grating line density. The problem of distance ambiguity at ranges that exceed the channel spacing in the complex multi-heterodyne spectrum can be mitigated either by a more sophisticated peak sorting and matching algorithms and multiple up-chirping and down-chirping ramps. Alternatively, distant objects can be obscured by matching the coherence length of the pump laser to the distance ambiguity range. Moreover, synchronous tuning of the pump laser and the microresonator, i.e. using monolithically integrated piezoelectrical frequency tuners [41] or frequency comb generation in electro-optical materials [17], serve to completely eliminate the residual nonlinearities of tuning that arise from the Raman self-frequency shift of the soliton and remove the requirement of high-power pumping while possibly extending the soliton existence range. Finally, and equally important, we believe that the first demonstration of frequency modulated dual solitons might be extended to other frequency comb sources as well as to other frequencies and will be applicable in the neighbouring fields of spectroscopy and in particular optical coherence tomography (OCT).

ACKNOWLEDGEMENTS

This material is based upon work supported by the Air Force Office of Scientific Research (AFOSR), Air Force Material Command, USAF under Award No. FA9550-15-1-0250. J.R. and acknowledges support from the EUs H2020 research and innovation program under Marie Skłodowska-Curie IF grant agreement No. 846737 (CoSiLiS). The authors thank Jeremie Renaudier of Nokia Bell labs for valuable suggestions. The Si₃N₄ samples were fabricated in the EPFL Center of Micro-NanoTechnology (CMi). The work was moreover supported by the Swiss National Science Foundation (SNF).

DATA AVAILABILITY STATEMENT

All data, figures and analysis code will be published on Zenodo upon publication of the work.

AUTHOR CONTRIBUTIONS

A.L. and J.R. conducted the various experiments and analyzed the data. A.L. designed the samples. J.L. fabricated the samples. All authors discussed the manuscript.

A.L., J.R., M.K. and T.J.K. wrote the manuscript. T.J.K. supervised the work.

* tobias.kippenberg@epfl.ch

- [1] C. Urmson, J. Anhalt, D. Bagnell, C. Baker, R. Bittner, M. Clark, J. Dolan, D. Duggins, T. Galatali, C. Geyer, *et al.*, *Journal of Field Robotics* **25**, 425 (2008).
- [2] H. Bostick, *IEEE Journal of Quantum Electronics* **3**, 232 (1967).
- [3] D. Uttam and B. Culshaw, *Journal of Lightwave Technology* **3**, 971 (1985).
- [4] R. Qian, K. C. Zhou, J. Zhang, C. Viehland, A.-H. Dhalla, and J. A. Izatt, *arXiv preprint arXiv:2008.05805* (2020).
- [5] T. Herr, V. Brasch, J. D. Jost, I. Mirgorodskiy, G. Lihachev, M. L. Gorodetsky, and T. J. Kippenberg, *Physical Review Letters* **113**, 1 (2014), 1311.1716.
- [6] T. J. Kippenberg, A. L. Gaeta, M. Lipson, and M. L. Gorodetsky, *Science* **361**, eaan8083 (2018).
- [7] J. Riemensberger, A. Lukashchuk, M. Karpov, W. Weng, E. Lucas, J. Liu, and T. J. Kippenberg, *Nature* **581**, 164 (2020).
- [8] A. Martin, D. Dodane, L. Leviandier, D. Dolfi, A. Naughton, P. O'Brien, T. Spuessens, R. Baets, G. Lepage, P. Verheyen, *et al.*, *Journal of Lightwave Technology* **36**, 4640 (2018).
- [9] S. Gao, M. O'Sullivan, and R. Hui, *Optics express* **20**, 25867 (2012).
- [10] M. A. Canuto, F. Estrada-Belli, T. G. Garrison, S. D. Houston, M. J. Acuña, M. Kovác, D. Marken, P. Nondédéo, L. Auld-Thomas, C. Castanet, D. Chatelain, C. R. Chiriboga, T. Drápela, T. Lieskovský, A. Tokovinine, A. Velasquez, J. C. Fernández-Díaz, and R. Shrestha, *Science* **361** (2018).
- [11] Y. Li and J. Ibanez-Guzman, *arXiv preprint arXiv:2004.08467* (2020).
- [12] N. Kuse and M. E. Fermann, *APL Photonics* **4**, 106105 (2019).
- [13] M.-C. Amann, *Electronics Letters* **28**, 1694 (1992).
- [14] C. Rogers, A. Y. Piggott, D. J. Thomson, R. F. Wiser, I. E. Opris, S. A. Fortune, A. J. Compston, A. Gondarenko, F. Meng, X. Chen, *et al.*, *arXiv preprint arXiv:2008.02411* (2020).
- [15] Y. Jiang, S. Karpf, and B. Jalali, *Nature Photonics* **14**, 14 (2020).
- [16] C. V. Poulton, M. J. Byrd, P. Russo, E. Timurdogan, M. Khandaker, D. Vermeulen, and M. R. Watts, *IEEE Journal of Selected Topics in Quantum Electronics* **25**, 1 (2019).
- [17] M. Zhang, B. Buscaino, C. Wang, A. Shams-Ansari, C. Reimer, R. Zhu, J. M. Kahn, and M. Lončar, *Nature* **568**, 373 (2019).
- [18] C. R. Doerr, *Frontiers in Physics* **3**, 37 (2015).
- [19] S. Schiller, *Optics Letters* **27**, 766 (2002).
- [20] F. Keilmann, C. Gohle, and R. Holzwarth, *Optics Letters* **29**, 1542 (2004).
- [21] I. A. N. Coddington, N. A. N. Ewbury, and W. I. S. Wann, **3** (2016).
- [22] I. Coddington, W. C. Swann, L. Nenadovic, and N. R. Newbury, *Nature Photonics* **3**, 351 (2009).

- [23] P. Trocha, M. Karpov, D. Ganin, M. H. P. Pfeiffer, A. Kordts, S. Wolf, J. Krockenberger, P. Marin-Palomo, C. Weimann, S. Randel, W. Freude, T. J. Kippenberg, and C. Koos, *Science* **359**, 887 (2018), 1707.05969.
- [24] M. G. Suh and K. J. Vahala, *Science* **359**, 884 (2018), 1705.06697.
- [25] F. R. Giorgetta, W. C. Swann, L. C. Sinclair, E. Baumann, I. Coddington, and N. R. Newbury, *Nature Photonics* **7**, 434 (2013).
- [26] H. J. Kim, D. E. Leaird, and A. M. Weiner, *IEEE Transactions on Microwave Theory and Techniques* **64**, 3351 (2016).
- [27] B. Lomsadze, B. C. Smith, and S. T. Cundiff, *Nature Photonics* **12**, 676 (2018), 1806.05071.
- [28] T. Ideguchi, S. Holzner, B. Bernhardt, G. Guelachvili, N. Picqué, and T. W. Hänsch, *Nature* **502**, 355 (2013), 1302.2414.
- [29] D. J. Moss, R. Morandotti, A. L. Gaeta, and M. Lipson, *Nature photonics* **7**, 597 (2013).
- [30] D. Pierrottet, F. Amzajerdian, L. Petway, B. Barnes, G. Lockard, and M. Rubio, *MRS Online Proceedings Library Archive* **1076** (2008).
- [31] F. Derr, *Electronics Letters* **27**, 2177 (1991).
- [32] K. Kikuchi, *Journal of Lightwave Technology* **34**, 157 (2015).
- [33] M. Karpov, H. Guo, A. Kordts, V. Brasch, M. H. Pfeiffer, M. Zervas, M. Geiselmann, and T. J. Kippenberg, *Physical Review Letters* **116**, 1 (2016).
- [34] X. Yi, Q.-F. Yang, K. Y. Yang, and K. Vahala, *Optics letters* **41**, 3419 (2016).
- [35] V. Brasch, M. Geiselmann, T. Herr, G. Lihachev, M. H. Pfeiffer, M. L. Gorodetsky, and T. J. Kippenberg, *Science* **351**, 357 (2016).
- [36] X. Yi, Q.-F. Yang, X. Zhang, K. Y. Yang, X. Li, and K. Vahala, *Nature communications* **8**, 1 (2017).
- [37] M.-G. Suh and K. Vahala, *Optica* **5**, 65 (2018).
- [38] J. Liu, E. Lucas, A. S. Raja, J. He, J. Riemensberger, R. N. Wang, M. Karpov, H. Guo, R. Bouchand, and T. J. Kippenberg, *Nature Photonics* , 1 (2020).
- [39] N. R. Newbury, I. Coddington, and W. Swann, *Optics express* **18**, 7929 (2010).
- [40] C. O. de Beeck, B. Haq, L. Elsinger, A. Gocalinska, E. Pelucchi, B. Corbett, G. Roelkens, and B. Kuyken, *Optica* **7**, 386 (2020).
- [41] J. Liu, H. Tian, E. Lucas, A. S. Raja, G. Lihachev, R. N. Wang, J. He, T. Liu, M. H. Anderson, W. Weng, *et al.*, *Nature* **583**, 385 (2020).
- [42] M. H. P. Pfeiffer, C. Herkommer, J. Liu, T. Morais, M. Zervas, M. Geiselmann, and T. J. Kippenberg, *IEEE Journal of Selected Topics in Quantum Electronics* **24**, 1 (2018).
- [43] J. Liu, A. S. Raja, M. Karpov, B. Ghadiani, M. H. P. Pfeiffer, B. Du, N. J. Engelsens, H. Guo, M. Zervas, and T. J. Kippenberg, *Optica* **5**, 1347 (2018), 1805.00069.
- [44] M. H. P. Pfeiffer, J. Liu, A. S. Raja, T. Morais, B. Ghadiani, and T. J. Kippenberg, *Optica* **5**, 884 (2018).
- [45] H. Guo, M. Karpov, E. Lucas, A. Kordts, M. H. Pfeiffer, V. Brasch, G. Lihachev, V. E. Lobanov, M. L. Gorodetsky, and T. J. Kippenberg, *Nature Physics* **13**, 94 (2017), 1601.05036.
- [46] M. Karpov, M. H. P. Pfeiffer, H. Guo, W. Weng, J. Liu, and T. J. Kippenberg, *Nature Physics* **15**, 1071 (2019).
- [47] T.-J. Ahn and D. Y. Kim, *Applied optics* **46**, 2394 (2007).
- [48] T. Hodgkinson, R. Harmon, and D. Smith, *Electronics Letters* **21**, 867 (1985).
- [49] A. Davis, M. Pettitt, J. King, and S. Wright, *Journal of lightwave technology* **5**, 561 (1987).
- [50] S. Ellingson, *Argus Technical and Scientific Documents* (2003).
- [51] P. Feneyrou, L. Leviandier, J. Minet, G. Pillet, A. Martin, D. Dolfi, J.-P. Schlotterbeck, P. Rondeau, X. Lacondemine, A. Rieu, *et al.*, *Applied optics* **56**, 9663 (2017).
- [52] N. Kuse, T. Tetsumoto, G. Navickaite, M. Geiselmann, and M. E. Fermann, *Optics Letters* **45**, 927 (2020).
- [53] D. M. Baney, P. Gallion, and R. S. Tucker, *Optical fiber technology* **6**, 122 (2000).

METHODS

Sample fabrication

Integrated Si₃N₄ microresonators are fabricated with the photonic damascene process [42]. Features are defined using deep-ultraviolet (DUV) stepper lithography [43] and reactive ion etching and silica preform reflow [44] prior to deposition reduces scattering losses. The waveguide width is 1.5 μm and its height is 0.82 μm, which leads to an anomalous second order dispersion of $D_2/2\pi = 1.13$ MHz and the third-order dispersion parameter is $D_3/2\pi = 576$ Hz. The positions of the resonance frequencies close to the pumped resonance are expressed with the series $\omega_\mu = \omega_0 + \sum_{i \geq 1} D_i \mu_i / i!$. The ring radius of the signal comb is 228.43 μm and results in a resonator free-spectral-range of $D_1/2\pi = 98.9$ GHz. The LO comb has similar cross-section and its radius is 227.27 μm, which leads to a free-spectral-range of 99.35 GHz. Both resonators are operated in the strongly overcoupled regime with intrinsic loss rate $\kappa_0/2\pi = 15$ MHz and bus waveguide coupling rate $\kappa_{\text{ex}}/2\pi = 100$ MHz in order to optimize comb output power and optical signal-to-noise-ratio after amplification. The radii of the 35 GHz samples are 645 μm and 648 μm resulting in $\Delta f_{\text{rep}} \approx 140$ MHz.

Dual FM soliton microcomb generation

We use an external cavity diode laser (ECDL) for our proof-of-principle, which is coupled to a dual Mach-Zehnder Modulator driven by a frequency-agile VCO and biased for single-sideband modulation. The laser is amplified, split and coupled into two photonic chips using lensed fibers and double inverse tapers [43]. Optical power incident on the each chip is ~2 W. Manual tuning with the EDCL piezo is used to tune into resonance. Upon traversing from blue to red, the chaotic modulation instability state collapses into a stable dissipative Kerr soliton [5] state. The thermal nonlinearity of Si₃N₄ facilitates the elimination of undesired multi-soliton states [45] when the laser-cavity detuning $\delta^{\text{sig,LO}}$ is reduced be-

yond the soliton existence range into the transient chaos region [46]. If both cavity resonances are aligned, the associated sudden drop in intracavity power increases the detuning δ of the switching comb, hence leapfrogging the detuning of the non-switching comb. The laser detunings are monitored using the phase modulation response technique introduced in [45] and temperatures of the samples are adjusted during the dual soliton switching process, if necessary using a thermal tuner. In this way, dual single soliton states can be obtained routinely and quickly. We subsequently optimize the laser-cavity detunings $\delta^{\text{sig,LO}}$ of signal and LO combs by thermal tuning to minimize the differential Raman shift and hence optimize linearity.

Linearization

The precision of coherent laser ranging is directly impacted by the linearity of the chirps that constitute the triangular frequency modulation. The chirp is applied to narrowband CW laser via single side-band modulator driven by a VCO. An iterative linearization algorithm was applied to the pump frequency chirp based on chirp measurement in an imbalanced Mach-Zehnder interferometer (MZI) [47]. The detailed procedure can be found in the Methods section of Ref. [7].

Parallel velocimetry and ranging

The experimental setup is illustrated in extended data Fig. 3a. The frequency modulation $1/T$ and excursion B of the pump laser are adjusted to 100 kHz and 1.55 GHz, respectively. A pump laser with triangular frequency modulation drives two distinct optical microresonators with slightly different radii, which serve as signal and LO in the experiment. After filtering (FBG) and amplification (EDFA), the signal comb is spatially dispersed over the target area using diffractive optics (transmission grating (966 lines/mm)). Each signal comb tooth μ represents an independent FMCW ranging channel measuring distance x_μ and velocity v_μ . The reflected signal is post-amplified similar to signals in high-bandwidth and long haul optical telecommunication systems and simultaneously superimposed with the amplified LO comb on a coherent receiver. A programmable filter (WS) is used to filter out excess (amplified spontaneous emission) ASE noise around the pump of the LO. A bistatic detection with separate collimators for the transmit and receive path is chosen to minimize spurious backreflection in the fiber components. Another balanced photodiode is used to calibrate Δf_{rep} and the channel-dependent frequency excursion B . A mirror galvanometer (shown in Fig. 3) is used to scan the dispersed light beams in the vertical direction.

The imaging experiment (Fig. 3) is carried out with

a signal soliton microcomb repetition rate of 98.9 GHz and repetition rate difference of 490 MHz. The in-phase (I) and quadrature (Q) signals from the coherent photoreceiver are recorded on a fast oscilloscope and processed offline. We utilize microcomb channels between $\mu = -15, +15$, where $\mu = 0$ denotes the pump frequency, while $\mu = 0, \pm 1$ are filtered out by the WS due to the excess of the ASE, resulting in 28 independent channels. All the data points are collected from a single trace covering 136 vertical lines. The galvo-scanner is set on a linear scan mode, while the oscilloscope is triggered in segmental acquisition mode with 10 μs segment scan time and 10 ms idle time between segments to allow the scanning Galvanometer enough time to rotate and capture the full scene. Overall, the measurement time is less than 1.5 seconds and was limited by the galvanometer response bandwidth, not the pixel sampling rate. The 3D point cloud of 136×28 pixels was obtained after post-processing. The test scene is presented in extended data Fig. 6. Chess figures are placed approximately one meter in front of the beam-splitter, the differential delay between signal and LO combs in optical fiber is around 27 m. The Pawn and Queen figurines are spaced 12 cm apart while the Queen and King figurines are spaced 14 cm apart. The required coherent receiver bandwidth for this configuration is determined as $\mu \Delta f_{\text{rep}} \approx 7.5$ GHz.

The velocimetry measurements are carried out with 35 GHz microcombs and 140 MHz Δf_{rep} allowing us to increase the number of operational channels $\mu = \pm 5, \pm 40$. Channels $\mu = -4, +4$ are filtered out by the WS due to the excess ASE. The frequency excursion B_μ ranges from 500 up to 950 MHz (extended data Fig. 3d), which results in decreased depth resolution compared to the previous 100 GHz soliton microcomb system. Mechanical vibrations of the flywheel not only impact distance and velocity precision, but also limit the total number of possible detections. In extended data Fig. 5, we present the detection statistics obtained over 190 μs continuous measurement time, i.e. 19 periods of the triangular waveform. Unfilled circles in panel a) (the same as in Fig. 4d) correspond to a measurement over one period with a mean number of detections equal to 56. Filled circles correspond to the data averaged over five periods. Panel b) depicts a probability for each channel to be detected. The roll-off at high $|\mu|$ originates from the limited optical amplification bandwidth. Panel c) represents the probability distribution of the sum of successfully detected pixels during individual scan periods, which is calculated by dividing the number of detections in a period over the full number of channels ($\mu = -40, +40$).

Coherent detection and post-processing

The frequency of the complex heterodyne beat note for the channel μ and a photon time-of-flight τ follows as the

difference between the instantaneous optical frequencies of signal and LO comb teeth $\nu_{\mu}^{\text{sig,LO}}$

$$\begin{aligned} f_{\mu}^{\text{IQ}}(t) &= \nu_{\mu}^{\text{LO}} - \nu_{\mu}^{\text{sig}} \\ &= \delta(t) + \mu f_{\text{rep}}^{\text{LO}}(t) - \delta(t + \tau) - \mu f_{\text{rep}}^{\text{sig}}(t + \tau). \end{aligned} \quad (2)$$

The first and third terms are similar to the case of single frequency coherent photoreceiver FMCW LiDAR [9]. In our case that frequency is offset by the repetition rate difference of the soliton microcombs multiplied by the channel number and adding the Doppler shift due to the relative target velocity v , we arrive at the following expressions:

$$\begin{aligned} f_{\mu}^{\text{u}} &= \mu \cdot (f_{\text{rep}}^{\text{sig}} - f_{\text{rep}}^{\text{LO}}) + \frac{B}{2T} \cdot \tau + \nu_{\mu} \cdot \frac{v}{c} \\ f_{\mu}^{\text{d}} &= \mu \cdot (f_{\text{rep}}^{\text{sig}} - f_{\text{rep}}^{\text{LO}}) - \frac{B}{2T} \cdot \tau + \nu_{\mu} \cdot \frac{v}{c}. \end{aligned} \quad (3)$$

According to our notation, positive frequencies in the complex RF spectrum correspond to optical carrier frequencies larger than the pump, negative frequencies to channels with smaller optical carrier frequencies than the pump. The distance and velocity can be inferred from these expressions and are depicted in the inset of Fig. 1 d.

Our coherent receiver consists of 90° optical hybrid coupler, two balanced photodetectors and subsequent RF amplifiers. This type of receiver is commonly referred as "phase-diversity homodyne receiver" [48, 49] or "intra-dyne receiver" [31]. It is similar to established receivers used in quadrature-amplitude modulation schemes that are employed in long haul optical communication systems. It allows full reconstruction of the amplitude and phase of the RF beat note between the signal and the LO and reveals distinct spectral information both in positive and negative RF frequencies. Due to the differential delays of discrete components and the response of the balanced photoreceivers and amplifiers, the in-phase (I) and quadrature (Q) signals are not perfectly orthogonal. We perform IQ imbalance correction [50], which substantially improves orthogonality (extended data Fig. 2). However, for higher channels mismatch still exists and one can observe 'images' on time frequency maps (i.e. Fig 2e left panel). The post-processing relies on short time Fourier transform over the half of the period to retrieve $f_{\mu}^{\text{u}}, f_{\mu}^{\text{d}}$ RF frequencies. In this regard, the 'image' peaks do not pose a problem, since we know that the positive frequencies will give a higher frequency beat note first while for the negative ones it would be the lower one (extended data Fig. 2). It is obtained by triggering data acquisition on the oscilloscope by function generator used to create the triangular frequency modulation control signal for the VCO. Distance information is obtained as a difference between $f_{\mu}^{\text{u}}, f_{\mu}^{\text{d}}$, while the mean offset of $f_{\mu}^{\text{u}} + f_{\mu}^{\text{d}}$ from $\mu \Delta f_{\text{rep}}$ is proportional to the velocity. Calculation of the Δf_{rep} is outlined below. Further improvements,

especially in long range detection can be achieved using active demodulation analysis [51].

Calibration of channel-dependent frequency excursion

In general, the soliton repetition rate f_{rep} depends on the laser cavity detuning, because of intrapulse stimulated Raman scattering [33, 34] and the soliton recoil effect associated with dispersive wave emission [35, 36]. During chirped soliton generation, this induces a change of the soliton repetition rate during each chirp cycle, which is observed in the form of a channel-dependent frequency excursion B_{μ} and chirp nonlinearity [7]. We observe that it does not depend strongly on the pump laser detuning and is independent of the pump power.

We measure the time-dependent chirp on both signal and LO combs and all channels by recording a heterodyne beat note with a second laser simultaneously on a pair of balanced photodetectors and a fast sampling oscilloscope (cf. Fig. 2a). For direct comparison of signal and LO chirps, we add the two beat note signals prior to short-time Fourier transform and depict both beat notes on a single panel. The full dataset corresponding to the subset of heterodyne beat signals presented in Fig. 2d is depicted in extended data figure 1. The amplitude of the triangular ramps decreases from positive to negative channels both for LO and signal. We retrieve the frequency excursion by fitting a symmetric triangular ramp to the time-dependent frequency of the heterodyne beat notes. The result of this analysis is plotted in Fig. 2f-i.

Heterodyne beat spectroscopy is well suited to characterize the chirp waveforms, but not practical for ranging and velocimetry, as it requires an independent reference laser. Hence, during the experiments presented in figures 3 and 4, we utilize a reference optical fiber MZI that is derived by tapping a fraction of signal and LO and beating them together on a second balanced photodiode (cf. extended data Fig. 3a). Inphase detection suffices, because Doppler-shifts are negligible in the reference MZI and all channels μ observe the same distance x_{μ} but different frequency excursions B_{μ} , which simplifies interpretation of the signal, which is plotted in extended data figure 3b.

Due to the channel-dependent excursion $\pm\mu$ channel would give a beat note consisting of four lines (cf extended data Fig. 3b), where two outer lines correspond to positive frequencies with higher excursion and two inner lines correspond to negative frequencies with lower excursion. Thus, we perform excursion inference for the 6 channels $\mu = \pm 1, \pm 3$ (that is allowed by 1.6 GHz bandwidth) and further extrapolate it considering linear dependence (cf. Fig. 2 f,h,i). For the 35 GHz chips we utilize channels $\mu = \pm 2, \pm 10$ for calibration. Knowledge of the pump excursion enables us to calculate the distance of MZI, while given distance one can obtain excursion

for channel μ from time-frequency analyzes. The same way one can infer channel-dependent excursion from real distance measurement if the distance to the target is the same for all of the channels (e.g. carton block). Furthermore, we can also calculate Δf_{rep} from the same calibration measurement. Since there is no Doppler shift, Δf_{rep} is equal to the mean of two beat notes divided by $|\mu|$. Hence, we are able to conduct the experiments with free-running soliton microcombs. Extended data Fig. 3c,d present comparison of the excursion inferred from the calibration measurement and further extrapolated and from a real distance measurement with a carton block. In the experiments described in the main part of the manuscript we utilized excursion and Δf_{rep} for velocity and distance calculations inferred from the calibration measurements.

Impact of nonlinear chirp transduction

Multiheterodyne mixing of dual-chirped soliton microcombs necessitates not only soliton generation to preserve chirp linearity from the pump to the comb teeth, but also requires that chirps are transduced equally, so as to avoid a difference in the frequency excursion B_μ between the signal and LO comb teeth that would broaden the ranging beatnote and penalize detection precision and sensitivity. We have two contributions effecting soliton repetition rate given change in pump frequency: the chromatic dispersion of the cavity D_2 , i.e. frequency dependency of the free-spectral-range D_1 , and Raman shift Ω [33, 34]. The overall change in repetition rate as a function of the detuning δ (frequency difference between the pump and 'cold' cavity resonance) can be written as

$$f_{\text{rep}}(\delta) = f_{\text{rep}}(0) + (\delta + \Omega(\delta)) \frac{D_2}{D_1}. \quad (4)$$

For dielectric integrated microresonators it is generally found that $\delta \ll \Omega(\delta)$ and hence the first term in the round brackets can be omitted. We also neglect the weak dependence of the free-spectral range and dispersion on the laser-cavity detuning that can be derived as $D_n(\delta) - D_n(0) \approx \delta \cdot D_{n+1}/D_1 \ll D_n(0)$. The linear dependence of the instantaneous f_{rep} on the laser-cavity detuning δ induces a channel-dependent frequency excursion B_μ without introducing nonlinearity into the triangular chirp [7]. Non-linear coupling between f_{rep} and f_{ceo} during the detuning sweep due to the soliton self-frequency shift leads to distortions of the triangular chirp. The nonlinear relation between the laser cavity detuning and the Raman soliton shift was derived in Ref. [34]:

$$\delta = \sqrt{\frac{15c\beta_2\omega_0}{32nQ} \frac{\Omega}{\tau_R} - \frac{c\beta_2}{2n} \Omega^2}, \quad (5)$$

where τ_R is Raman shock time and $\beta_2 = -\frac{n}{c} D_2/D_1^2$ is the chromatic dispersion term. Extended Data Fig. 4 a,b depict the time-varying detuning $\delta(t)$ of a triangular chirp

sequence of the pump laser and the Raman induced soliton self-frequency shift $\Omega/2\pi$ caused by the variation of the detuning. Extended Data Fig. 4 c depicts the induced variation of f_{rep} (blue) and Δf_{rep} component (red). We investigate the degradation of chirp linearity and similarity between the signal and LO combs due to the Raman effect as function of their respective and in general dissimilar detunings $\delta^{\text{sig,LO}}$ by inserting the Raman induced periodic change of f_{rep} into equations 2 and 3. We distinguish the cases of vanishing and modest differential detunings $\Delta\delta = \delta^{\text{sig}} - \delta^{\text{LO}} = 10\text{MHz}$ (cf. Fig. 4 d,e,f). The small difference in f_{rep} between signal and LO microcombs results in different Raman shifts, which causes frequency excursions to differ between the signal and LO combs on the scale of 1 MHz, which is comparable to the induced chirp nonlinearities of pump to sideband chirp transduction (extended data Fig. 4 c,e,f). To finally determine the signal degradation due to the soliton induced Raman self-frequency shift, we simulate the full signal generation and coherent detection chain at a distance of 30 m with a custom MATLAB script and apply the same data analysis techniques to the artificial (i.e. numerically generated) multiheterodyne LiDAR trace as for the real data. The resulting time frequency traces are depicted in extended data figure 4 g,h,i for the pump and the 15th low and high frequency comb teeth. The overall manifestation of the soliton Raman self-frequency shift induced nonlinearity can be seen in the tilt and curvature of the time dependent complex RF beat note frequency. The effects of the nonlinearities are exacerbated for channels further away from the pump (as the absolute frequency shift of a given comb teeth due to the Raman induced change in the soliton repetition rate multiplies with the relative mode number from the pump). The curvature that is imposed by the nonlinear component of the Raman frequency shift leads to a bias of the measured distances that increases with length difference between the target and the calibration MZI, differential detuning $\Delta\delta$ and channel number (cf. extended data figure 4 j,k,l,m). In the experiments presented here, we equalize MZI delays both in measurement and calibration interferometers (i.e. minimize differential delay), so that impact of Raman nonlinearities is similar for calibration and real measurement traces. In a real-world deployment of our system, a feed-forward scan scheme [41] or phase-locking the comb to a tuned resonator [52] to avoid detuning-dependent changes of the microcomb repetition rates would be favorable, and are possible to avoid this effect. Co-integration of both microcomb resonators on a single chip to avoid differential frequency drift is equally straightforward.

Signal-to-noise ratio of multiheterodyne FMCW LiDAR

A significant advantage of heterodyne detection is that it can approach the photon shot noise limit of detection and attain single photon sensitivities for low signal powers on a conventional semiconductor photodiode, if sufficient LO power is supplied for amplification. In the multiheterodyne case all individual channel LO are impinging on a small number of photodiodes (4 in case of a phase diversity receiver with balanced photodiodes). Generally, for a heterodyne LiDAR detection $P^{\text{LO}} > P^{\text{sig}}$ and the shot noise (mainly contributed by the LO) is a dominating source of noise (i.e., higher than the thermal noise) if sufficient LO power is supplied to the photodiode.

$$\text{SNR} = \frac{\langle I^2 \rangle}{\langle \Delta I^2 \rangle} = \frac{P^{\text{sig}}}{\hbar\omega\Delta\text{BW}} \quad (6)$$

Where ΔBW is the resolution bandwidth of the analysis FFT. For simplicity, we consider quantum efficiency of the photodiode to be 100%, thus the electric current is $I = RP = \frac{e}{\hbar\omega}P$. If an optical amplifier is used, than for the shot noise limited detection the total SNR would be at least 3dB lower:

$$\text{SNR} = \frac{P^{\text{sig}}}{2\hbar\omega\Delta\text{BW}} \quad (7)$$

Below we elaborate a more detailed analyzes for the case of multiple channels detected on a single balanced photodiode. Consider N distinct signal-LO channels distributed over the photodiode bandwidth with equal powers of the signal channels $P_\mu^{\text{sig}} = P^{\text{sig}}$ and LO channels $P_\mu^{\text{LO}} = P^{\text{LO}}$ for $\mu \in [1, N]$. For heterodyne detection the photodiode current of channel μ is $2R^2P^{\text{LO}}P^{\text{sig}}$, while the total noise $\langle \Delta I^2 \rangle$ effecting channel μ would consist of shot noise, thermal noise, spontaneous-spontaneous beating noise, and signal/LO-spontaneous beating noise [53].

The photon shot noise is proportional to the mean current impinging on the photodiodes

$$\begin{aligned} \sigma_{\text{sh}}^2 &= 2q\langle I \rangle\Delta\text{BW} \\ &= 2qR(NGP^{\text{LO}} + NGP^{\text{sig}} + P_{\text{ase}}^{\text{LO}} + P_{\text{ase}}^{\text{sig}})\Delta\text{BW} \quad (8) \\ &\approx 2qRNGP^{\text{LO}}\Delta\text{BW} \end{aligned}$$

mainly contributed by N LOs. Where P_{ase} is spontaneous emission noise and it equals $\rho_{\text{ase}}\Delta\nu_{\text{amp}} = n_{\text{sp}}\hbar\omega(G-1)\Delta\nu_{\text{amp}}$ with the amplification bandwidth $\Delta\nu_{\text{amp}}$ (4 THz for EDFA) and the spontaneous emission factor $n_{\text{sp}} = 1$ for the amplifier with complete inversion, q is the electron charge. Additionally, we consider equal gains for the detector pre-amplifiers of the signal and local oscillator microcombs $G^{\text{LO}} = G^{\text{sig}} = G$.

We consider the thermal noise of the photodiodes at room temperature

$$\sigma_{\text{th}}^2 = 4\frac{kT}{Z}\Delta\text{BW} \quad (9)$$

where kT is a thermal energy and the impedance Z of the load is 50 Ohm. Spontaneous-spontaneous and signal/LO-spontaneous beating noises include cross terms only, because we employ balanced photodetection,

$$\sigma_{\text{sp-sp}}^2 = 4R^2\rho_{\text{ase}}^{\text{sig}}\rho_{\text{ase}}^{\text{LO}}\Delta\nu_{\text{amp}}\Delta\text{BW}, \quad (10)$$

$$\sigma_{\text{sig/LO-sp}}^2 = 4R^2(NGP^{\text{LO}})\rho_{\text{ase}}^{\text{sig}}\Delta\text{BW} \quad (11)$$

$$+ 4R^2(NGP^{\text{sig}})\rho_{\text{ase}}^{\text{LO}}\Delta\text{BW}. \quad (12)$$

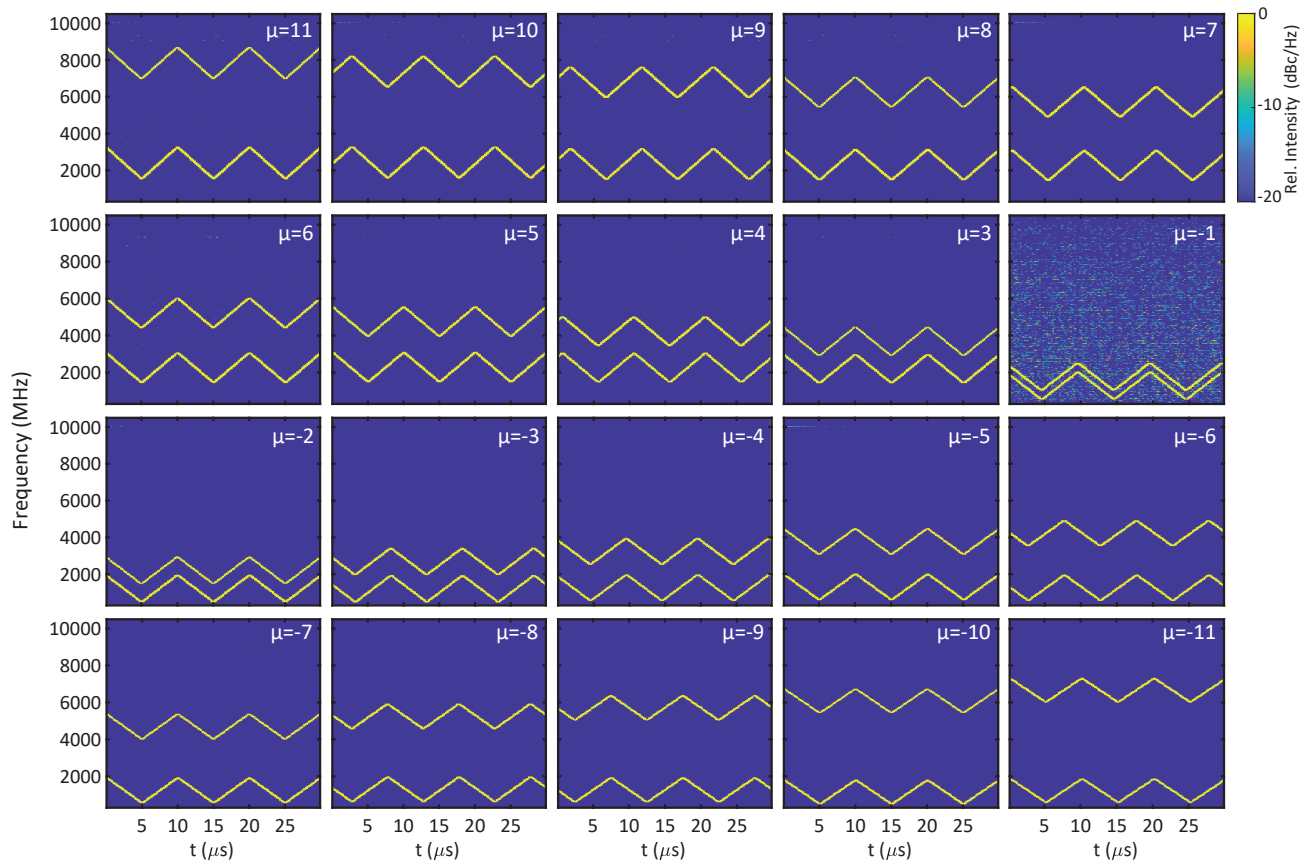
In the experiment, we use two optical amplifiers for the signal comb: a booster-amplifier before free-space emission and a detection pre-amplifier after light collection. In the above equations, P^{sig} denotes the optical power of the signal comb line at the input of the 90° optical hybrid. The ASE noise of the booster amplification stage is irrelevant in the coherent ranging application, as the optical loss in free space (> 60 dB) generally surpasses the single stage amplification gain. Thus the photon shot noise would be dominating at the post-amplification stage. Combining all noise terms and neglecting minor contributions, we determine the SNR for a given channel:

$$\text{SNR}_\mu = \frac{\langle I_\mu^2 \rangle}{\sigma_{\text{sh}}^2 + \sigma_{\text{th}}^2 + \sigma_{\text{sp-sp}}^2 + \sigma_{\text{sig/LO-sp}}^2} \quad (13)$$

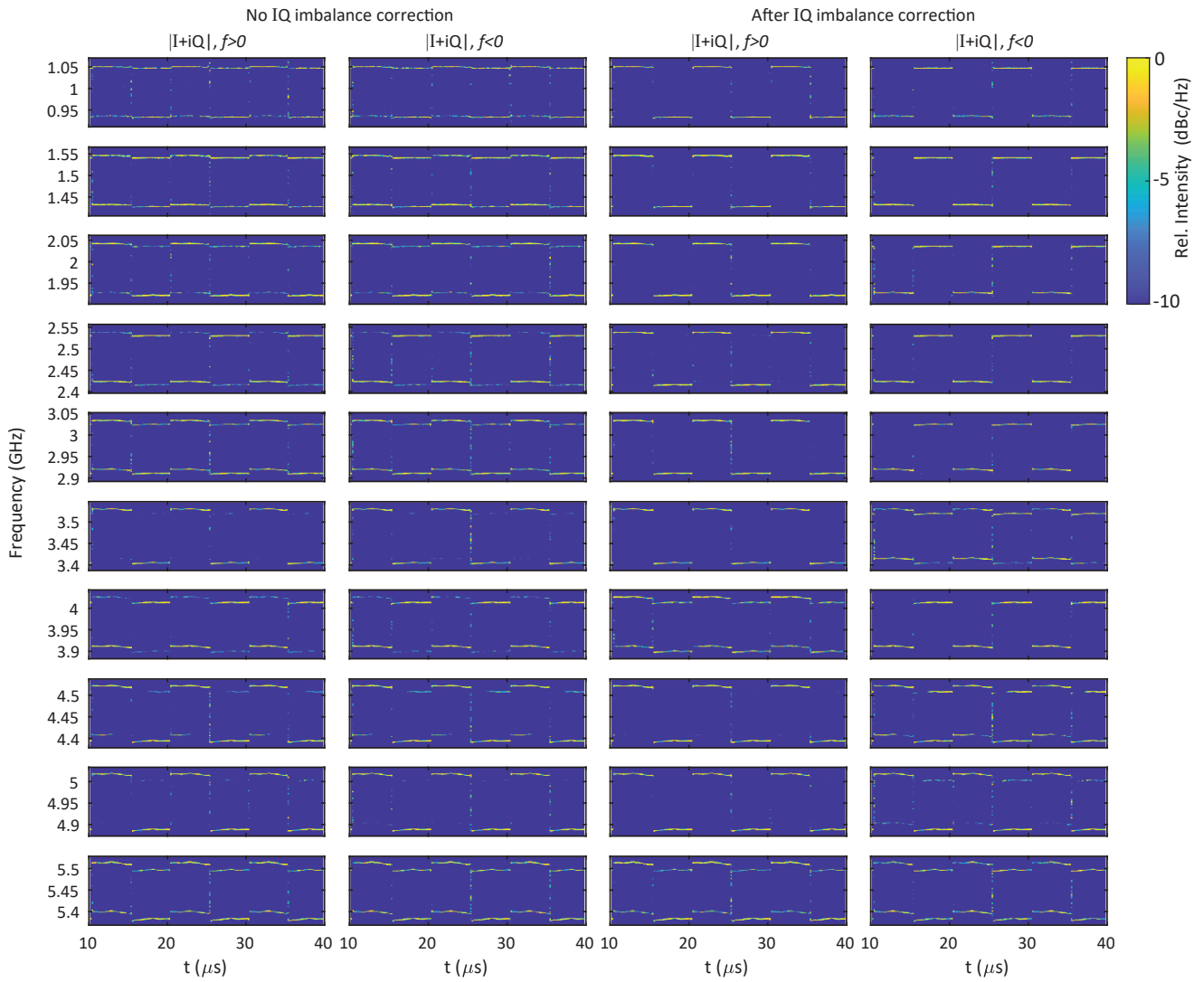
$$\approx \frac{2R^2P^{\text{sig}}P^{\text{LO}}}{4R^2(NGP^{\text{LO}})\rho_{\text{ase}}^{\text{sig}}\Delta\text{BW}} \approx \frac{P^{\text{sig}}}{2N\hbar\omega\Delta\text{BW}} \quad (14)$$

Thus, in the case of shot-noise limited operation, the SNR of a channel μ is reduced by the shot noise of the additional local oscillators and N times lower than in case of its detection on N separate photodetectors. This multiheterodyne penalty is well known in the realm of dual comb spectroscopy [39] and amounts to 17 dB for 50 channels. It can be reduced by spectral slicing or interleaving.

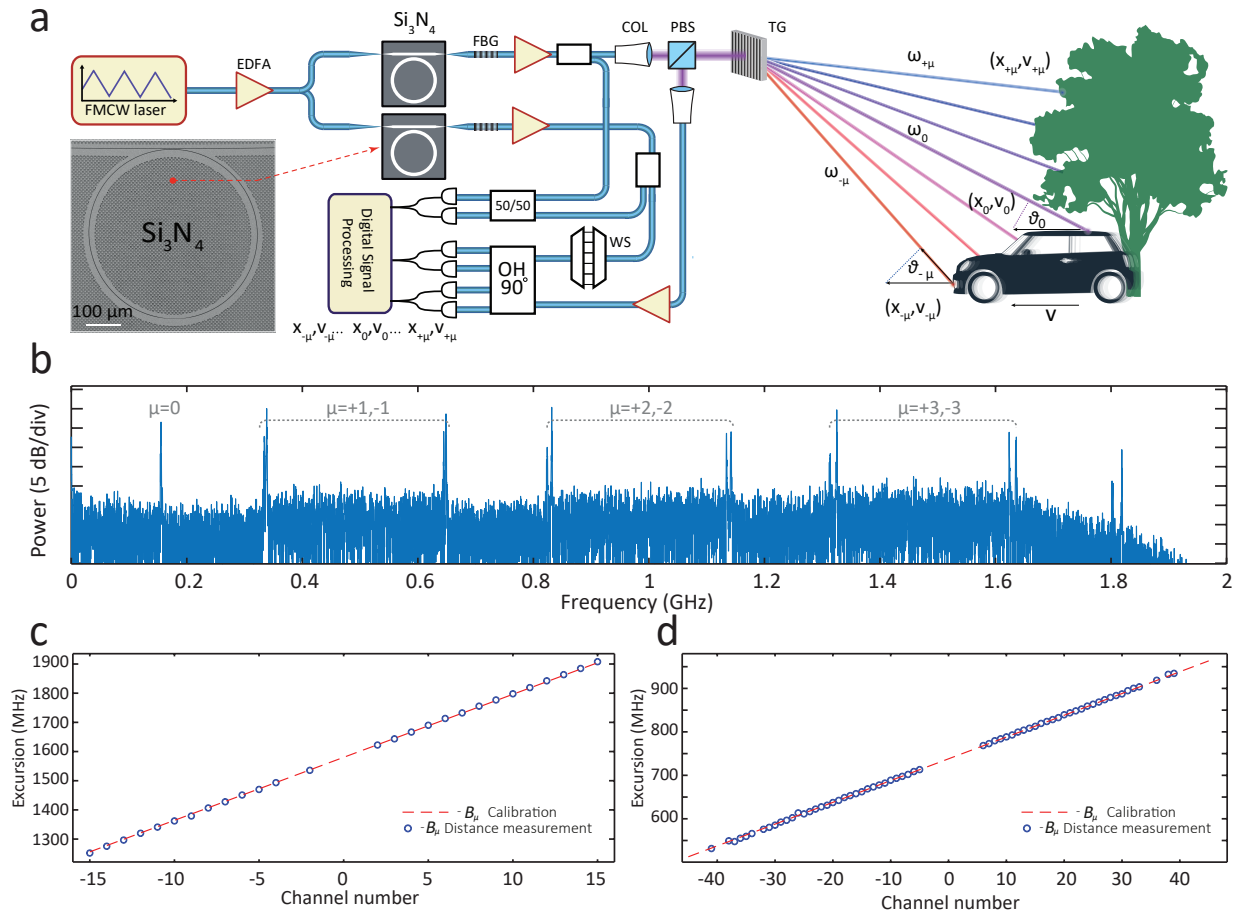
EXTENDED DATA FIGURES



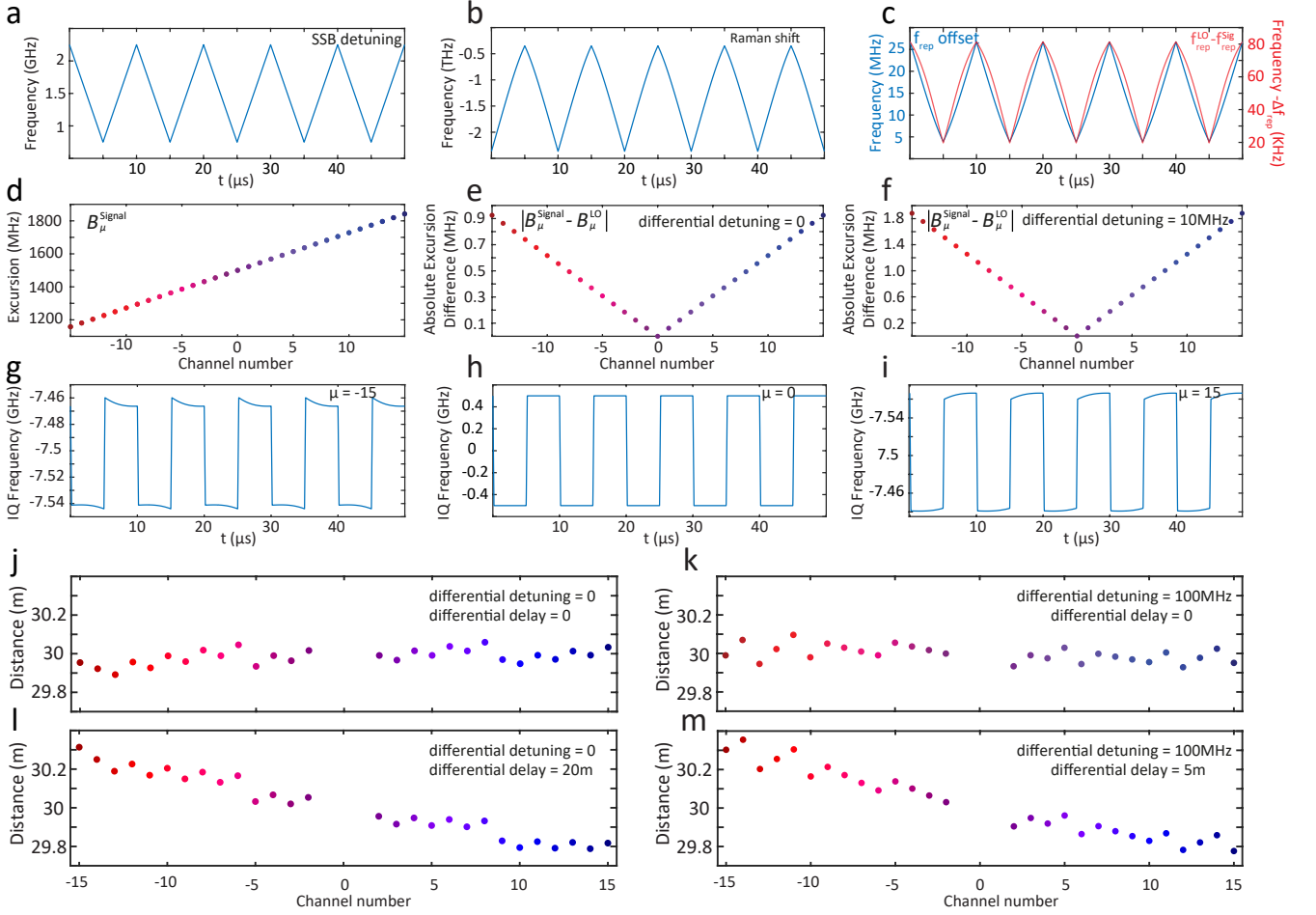
Extended Data Fig. 1. Heterodyne measurement of FMCW Dual-Comb Time-frequency map of heterodyne beat spectroscopy of signal and LO microcombs with external reference obtained by short-time Fourier transform with resolution bandwidth 2.45 MHz. Depicted here is the full data set corresponding to Fig. 2d of the main manuscript.



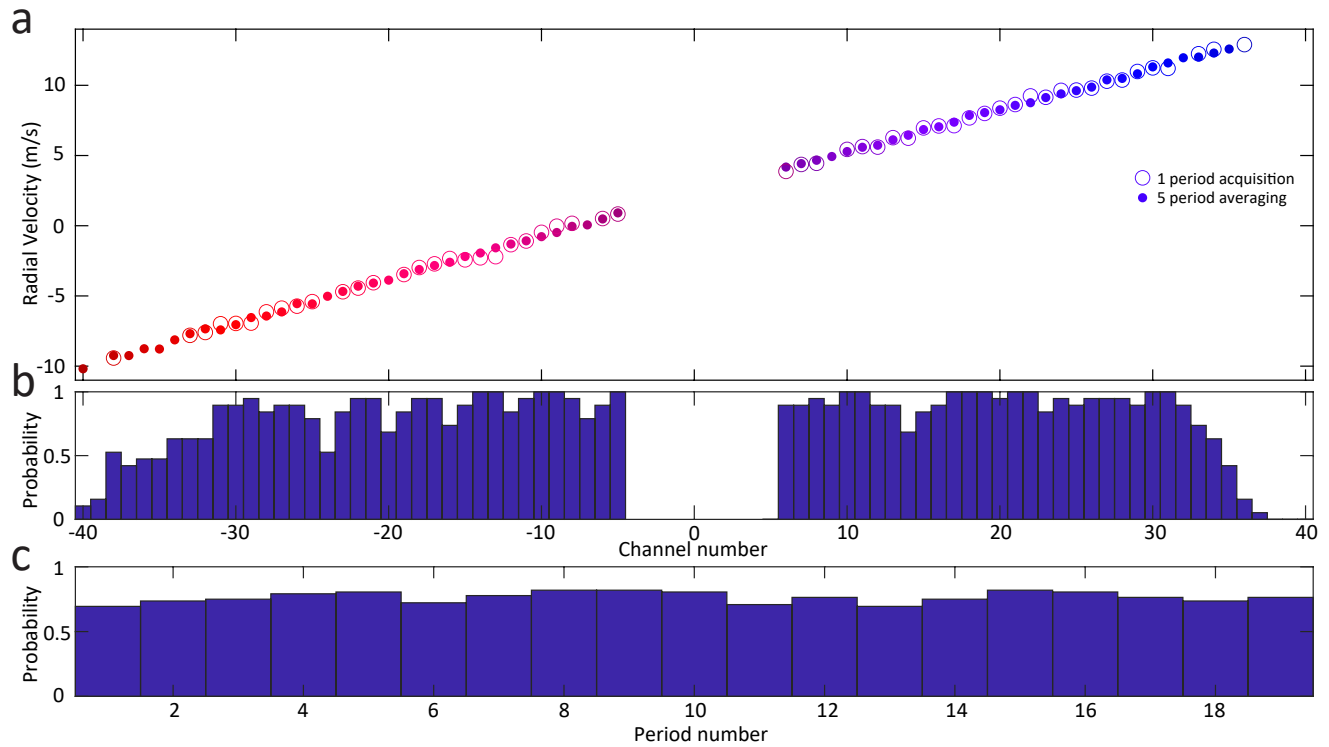
Extended Data Fig. 2. IQ imbalance correction Time-frequency map of delayed heterodyne beat spectroscopy for $\mu = \pm 2, \pm 11$. First two columns correspond to positive and negative channels without IQ imbalance correction, while second two columns are with IQ imbalance correction. ENBW 2.45 MHz.



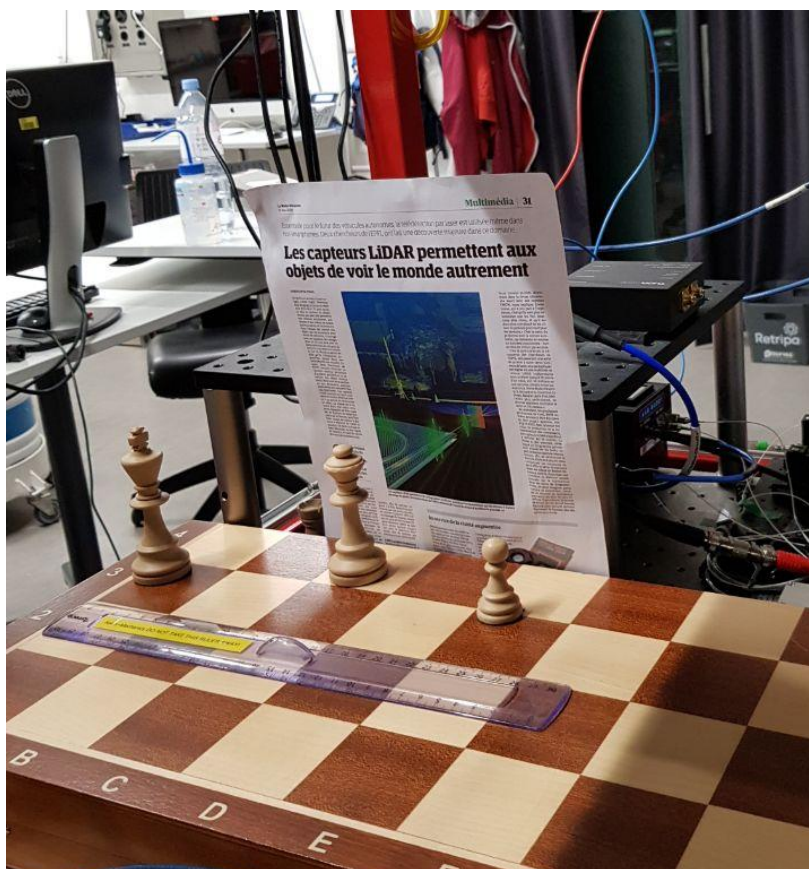
Extended Data Fig. 3. Excursion calibration a) Architecture of the multiheterodyne parallel FMCW LiDAR. A pump laser with triangular frequency modulation drives two distinct optical microresonators with slightly different radii, which serve as signal and LO in the experiment. After pump filtering (FBG) and amplification (EDFA), the signal comb is spatially dispersed over the target area using diffractive optics. Each signal comb tooth μ represents an independent FMCW ranging channel measuring distance x_μ and velocity v_μ . All channels are simultaneously superimposed with the amplified LO comb on a coherent receiver. Waveshaper (WS) is used filter out excess ASE noise around the pump of the LO. Extra reference balanced photo-diode is used to measure frequency excursion. b) Interferogram of a LO and signal combs beating recorded over one period ($10\mu\text{s}$) on the reference photodiode with 1.6GHz bandwidth. Beatings of 6 channels ($\mu = \pm 1, \pm 3$) allow Δf_{rep} and B_μ to be retrieved and used for the processing of the measured data. c) Two frequency excursion measurements with 100 GHz chips. Red dashed line is an extrapolation of excursion obtained from the reference delayed heterodyne measurement. Blue circles correspond to an excursion obtained from a lidar distance measurement of a carton block, where all the distances are the same for distinct channels. d) Same as c), but with 35 GHz chips



Extended Data Fig. 4. Raman nonlinearity impact in 100 GHz resonators a) Simulation of a pump cavity detuning representing a triangular ramp. b) Simulation of a Raman shift experienced by a Soliton while being frequency swept. c) Blue - f_{rep} offset from a 100GHz caused by Raman nonlinearities. Red - Δf_{rep} offset from a 500 MHz (100 and 100.5 GHz free spectral ranges were used in this simulation) for the two solitons while being frequency swept due to Raman nonlinearities. d) Simulated frequency excursion for 100 and 100.5 GHz resonators due to Raman effect. e,f) Simulated absolute frequency excursion difference considering soliton-cavity detuning to be the same for two resonators and have 10 MHz difference correspondingly. g,h,i) Simulated time-frequency maps obtained from a beating of signal and LO combs. Difference in excursion due to Raman effect results in deformed trapezoidal traces. Channels $\mu = -15, 0, +15$ correspondingly. j,k,l,m) Simulated distance measurements calculated from time-frequency maps above. The term differential delay stands for the difference between optical delay of signal and LO for the real measurement on one side and optical delay of signal and LO for the reference calibration measurement on the other side.



Extended Data Fig. 5. Velocimetry measurements statistics a) Multichannel velocity measurement for the flywheel rotating at around 200 Hz for a single $10 \mu\text{s}$ scan (open circles) and five frame stacking (filled circles). b) Probability of a pixel to be detected in channel μ . Statistics are obtained over 19 periods measurement time ($190 \mu\text{s}$). The roll-off at large distance from the pump laser originates from the limited optical amplifier bandwidth. c) Probability of detection over a given time frame ($10 \mu\text{s}$). The probability is calculated as number of total pixels detected in that time frame divided by 81 ($\mu = -40, +40$).



Extended Data Fig. 6. Photograph of the imaged scene Pawn, Queen and King chess figures used for the lidar distance measurement.